

Skeleton as a probe of the cosmic web: the 2D case

Dmitri Novikov,¹ Stéphane Colombi,² Olivier Doré^{2,3}

¹ *Astrophysics, University of Oxford, Denys Wilkinson Building, Keble Road, Oxford OX1 3RH, England*

² *Institut d'Astrophysique de Paris, 98 bis boulevard Arago, 75014 Paris, France*

³ *Department of Astrophysical Sciences, Princeton university, Peyton Hall, Ivy Lane, Princeton, NJ 08544, USA*
novikov@astro.ox.ac.uk, colombi@iap.fr, olivier@astro.princeton.edu

3 June 2018

ABSTRACT

We discuss the skeleton as a probe of the filamentary structures of a 2D random field. It can be defined for a smooth field as the ensemble of pairs of field lines departing from saddle points, initially aligned with the major axis of local curvature and connecting them to local maxima. This definition is thus non local and makes analytical predictions difficult, so we propose a local approximation: the *local* skeleton is given by the set of points where the gradient is aligned with the local curvature major axis and where the second component of the local curvature is negative.

We perform a statistical analysis of the length of the *total* local skeleton, chosen for simplicity as the set of all points of space where the gradient is either parallel or orthogonal to the main curvature axis. In all our numerical experiments, which include Gaussian and various non Gaussian realizations such as χ^2 fields and Zel'dovich maps, the differential length is found within a normalization factor to be very close to the probability distribution function of the smoothed field. This is in fact explicitly demonstrated in the Gaussian case.

This result might be discouraging for using the skeleton as a probe of non Gaussianity, but our analyses assume that the total length of the skeleton is a free, adjustable parameter. This total length could in fact be used to constrain cosmological models, in CMB maps but also in 3D galaxy catalogs, where it estimates the total length of filaments in the Universe. Making the link with other works, we also show how the skeleton can be used to study the dynamics of large scale structure.

1 INTRODUCTION

The observed large scale distribution of galaxies presents remarkable structures, such as clusters of galaxies, filaments, sheets and large voids. It is widely admitted that these structures grew from small initial fluctuations through gravitational instability. At very large scale, the filamentary pattern seen in the cosmic web is expected to be similar to that of the initial field (e.g., Bond, Kofman & Pogosyan 1996). Since these primordial inhomogeneities also imprinted the temperature fluctuations seen now in the Cosmic Microwave Background (CMB), the characterization of the observed large scale structures both in galaxy catalogs and in CMB maps can help to probe the nature of these primordial fluctuations, in particular whether they are Gaussianly distributed or not. Furthermore, a rigorous topological description of the observed structures is necessary to constrain efficiently models of large scale structure. For instance, a precise definition is needed for clusters of galaxies before inferring any constraints from their studies, e.g density and temperature profiles but also luminosity function and clustering. Analogously, a precise and practical definition of filaments would allow us to use them similarly as cluster of galaxies.

Various methods have been proposed to characterize the morphology of large scale structures. In general, one

studies the topological properties of excursion sets, i.e. regions below or above a density threshold. The statistics most explored up to now are the genus or the closely related Euler characteristic (see, e.g., Doroshkevich 1970; Gott, Melott & Dickinson 1986), the more complete set of observables given by Minkowski functionals (see, e.g., Mecke, Buchert & Wagner 1994) and related statistics such as shape finders (e.g., Sahni, Sathyaprakash & Shandarin 1998), but also estimators based on percolation analysis (see, e.g., Zel'dovich 1981; Zel'dovich, Einasto & Shandarin 1982; Shandarin 1983; Bhavsar & Barrow 1983) and minimum spanning tree construction (e.g., Barrow, Bhavsar & Sonoda 1985), such as for example structure functions or related shape estimators based on moments of inertia (see, e.g., Babul & Starkman 1992).

In general, topological descriptors are primarily used to constrain the level of non Gaussianity in the sample, since there often exists analytical predictions in the Gaussian case (see, e.g., Doroshkevich 1970 for the genus; Tomita 1986 for the Minkowski functionals). To do so, other estimators exist also, based on spatial correlation analysis, such as higher-order correlation functions in real or Fourier/harmonic space (e.g., Peebles 1980 and references therein), the probability distribution function (pdf) of the smoothed density field and

arXiv:astro-ph/0307003v1 30 Jun 2003

its moments (e.g., Bernardeau et al. 2002 and references therein), higher order moments the wavelet coefficients (e.g., Aghanim & Forni 1999; Hobson, Jones & Lasenby 1999), peak and excursion set subcomponents statistics (see, e.g., Bardeen et al. 1986; Bond & Efstathiou 1987 and Doré *et al.* 2003 for a somewhat related statistic), phase correlation analysis (e.g., Chian & Coles 2000; Naselsky, Novikov & Silk 2002), etc. In principle, all these statistics combine the data in very specific ways, so they altogether provide complementary analysis of the data.* However, at variance with traditional statistical estimators, topological estimators help as well to characterize in a very intuitive way the topology of structures in terms of filaments, sheets, clusters and voids quantitatively. For instance, the Minkowski functionals provide a complete basis of simple estimators to estimate the morphology of an excursion set (see, e.g., Kerscher 2000 for a review on the subject), e.g. its degree of compacity and of filamentarity.

In this paper we focus on the skeleton, which aims at extracting from the cosmic web its filamentary pattern. More specifically, the goal is to draw in the observed structure a set of lines which reproduces well the filamentary pattern guessed by eyes. A natural tool to do so in set of points such as galaxy catalogs is the minimum spanning tree (e.g., Barrow, Bhavsar & Sonoda 1985). It is a connected structure superposed to the set of points, with no loop and which is the shortest possible. Of course, using the minimum spanning tree as such is not very helpful since it is highly irregular and it is difficult to establish a link to the large scale features of interest, but there are technics to filter small scale noise consisting in “peeling” the tree, i.e. removing from it short branches. Even if it is successful in extracting the main filamentary features from the catalog,[†] the minimum spanning tree remains by nature unsmooth and difficult if not impossible to manipulate in order to perform analytic calculations.

The technique we aim to employ in this paper to extract the skeleton from the data sample is completely different and relies on Morse theory (see, e.g., Milnor 1963; Colombi, Pogosyan & Souradeep 2000; Jost 2002). It requires the field to be sufficiently differentiable and non degenerate as explained more in details later and thus some smoothing with e.g. a Gaussian window of the data file is necessary to use such technique.[‡] §

* see, e.g., Shandarin 2002 for a comparison of the pdf and the Minkowski functionals as estimators of non Gaussianity in 2D maps; Phillips & Kogut 2001 for a comparison between genus, extrema correlation function and bispectrum; Barreiro, Martínez-González & Sanz 2001 for a comparison between number density, eccentricity and Gaussian curvature of hot spots, and genus as estimators to probe non-Gaussianity in CMB samples.

[†] see, e.g. Fig. 1 of Doroskevich et al. 2001 for a nice illustration on the Las Campanas Redshift Survey.

[‡] note that the concept of smoothing introduce a scale in the problem: smoothing at different scales will not produce the same skeleton but will have interesting links to dynamics as discussed in the end of this paper.

§ Hence, at variance with the minimum spanning tree method, which has the advantage to deal directly with the discrete nature of galaxy sample, our method will be difficult to apply to real galaxy catalogs unless smoothing at sufficiently large scales.

We shall see that the skeleton can then be then rigorously defined as a set of pairs of special field lines departing from saddle points. The problem is that the skeleton defined as such is non local: indeed, to draw any field line, one has to resolve the trajectory of a particle following the equation of motion given by $d\mathbf{r}/dt = \nabla\rho$. This non local nature of the skeleton makes analytic predictions rather difficult. Furthermore, as discussed in Appendix A, it is difficult to find a reliable algorithm to draw it.

The main points of this paper, which focusses on the 2D case, are the following: (i) find a local approximation of the skeleton to address the issues just raised above, (ii) test this local approximation as a statistical tool to probe non Gaussian features of the density field in e.g. CMB maps, (iii) establish the link to dynamics. The last point will be only treated superficially through simple illustrative examples, relying mostly on the Zel’dovich approximation (Zel’dovich 1970), since it is clearly more interesting to treat it in detail in the 3D case.[℘]

This paper is thus organized as follows. In Section 2, We define the skeleton in the framework of Morse theory and discuss some of its properties. We find a local approximation to it, relying on two independent methods. This *local* skeleton is contained in the set of points of space where the gradient of the density field is aligned with one axis of the local curvature, that we call the *total* local skeleton. We show through examples that the local skeleton and the real skeleton are quite alike, both by visual inspection and by comparing their respective lengths and we discuss the differences found. In Section 3, we study the differential length of the total local skeleton as a function of density threshold. We find experimentally that it scales very much like the pdf of the smoothed density field, a property that we demonstrate explicitly in the Gaussian case. Finally, Section 4 discusses the results and makes the link to dynamics. An extensive appendix discusses the numerical calculations of this paper, which were performed with a dedicated package.

2 THE SKELETON OF A 2D RANDOM FIELD

In a two-dimensional field, one would naturally define the skeleton as a set of ridges connecting local maxima and separating under-dense regions. In what follows, we first give the practical mathematical definition corresponding to this view (§ 2.1). It is shown that the skeleton is a set of special field lines, i.e. a particular set of curves parallel to the gradient of the field, and passing through maxima and saddle points. However this definition is not very practical at least from the theoretical point of view, because it is non local and makes analytic predictions difficult. To enforce locality, we define an other set of curves that is aimed to be close to the real skeleton (§ 2.2). To do so we use two different approaches, which actually end in the same definition for the local skeleton. The first one consists in Taylor expanding the

[℘] Note however, that dynamics in 2D can be still of interest, particularly in relation to reconstruction of the projected mass distribution in weak lensing experiments: for instance the skeleton can be used as a tool to test the quality of the reconstruction methods.

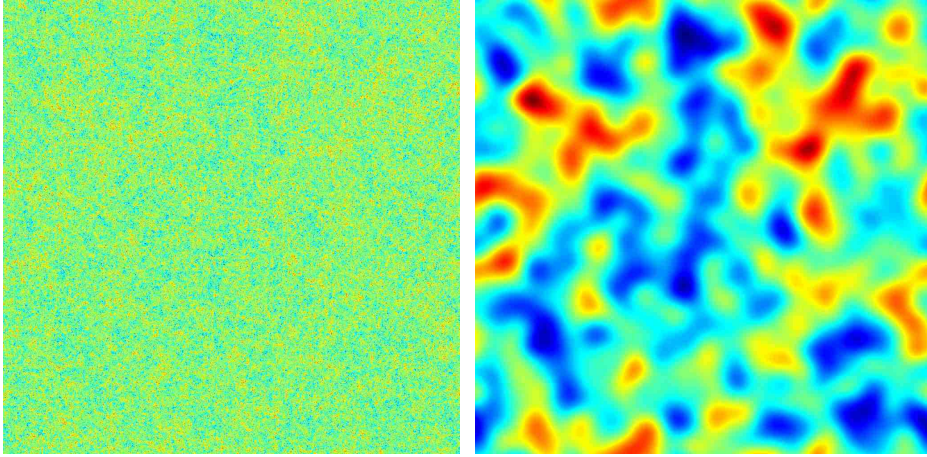


Figure 1. An example of Gaussian field and its smoothed counterpart.

Left panel: a periodic realization of a 2D Gaussian random field on a grid of size 1024×1024 pixels with a scale-free power-spectrum, verifying $P(k) \propto k^n$ with $n = -1$.

Right panel: the same field smoothed with a Gaussian window of radius 25 pixels.

special field lines in the neighborhood of saddle points and local maxima while the second one consists in finding points along isocontour lines such that the gradient of the density field has extremal magnitude. In § 2.3, our arguments will be illustrated by practical examples on a Gaussian field and its Zel’dovich mapping. As a probe of the local skeleton, in addition to visual inspection, we shall compare, for the examples considered here, its length as a function of density threshold with the length of the real skeleton.

In what follows, we consider a 2D random field, $\rho(\mathbf{r})$, e.g. a temperature map of the CMB. To assume sufficient differentiability we convolve it with a gaussian window of size ℓ , as illustrated by Fig. 1. The smoothed field, still noted ρ , is furthermore supposed to be sufficiently non degenerate, and in particular has the following properties:

(i) Its gradient cancels in a discrete set of critical points, which can be separated into three subclasses, local minima, local maxima and saddle points;

(ii) The eigenvalues $\lambda_1 \geq \lambda_2$ of its Hessian, $\mathcal{H} \equiv \partial^2 \rho / \partial r_i \partial r_j$, verify the following properties: the regions of space where $\lambda_1 = 0$ or where $\lambda_2 = 0$ are sets of smooth curves never passing through critical points. The intersection of these two sets of curves, where $\lambda_1 = \lambda_2 = 0$, is therefore a discrete set of points not containing any critical point.

Given these last definitions for λ_1 and λ_2 , the local maxima, saddle point and local minima verify respectively $0 > \lambda_1 \geq \lambda_2$, $\lambda_1 > 0 > \lambda_2$ and $\lambda_1 \geq \lambda_2 > 0$.

2.1 Definition

We first define the peak patches (void patches) as the regions of space containing all the points converging to the same local maximum (local minimum) while going along the field lines in the direction (opposite direction) of the gradient, $\nabla \rho \equiv \partial \rho / \partial r_i$.

The skeleton (of over-dense regions) is defined as the borders of the void patches (and a dual skeleton can be similarly defined as the borders of the peak patches). It is

easy to show that it passes through all the saddle points and the local maxima. It would be out of the scope of this paper to go further in the mathematical details of the topology of the skeleton, but one can list the following well known properties, valid only if there is no unexpected degeneracies (e.g., Jost 2002), and which can be easily verified by visual inspection of Fig. 2 (top left panel):

- The nodes of the skeleton are the local maxima, where multiple lines of the skeleton can converge. In general, because $\lambda_1 > \lambda_2$, these lines tend to converge along the axis aligned with the eigenvector associated to λ_1 (Fig. 3, left panel).
- Two local maxima cannot be directly connected together, there is always a saddle point in between;
- Saddle points cannot be nodes of the skeleton. Indeed, there are only four field lines connected to each saddle point: two unstable fields lines arriving from opposite directions, locally parallel to the eigenvector corresponding to $\lambda_2 < 0$, and two stable fields lines departing in opposite directions locally parallel to the eigenvector corresponding to $\lambda_1 > 0$ (Fig. 3, right panel). These two last field lines locally coincide with the skeleton and end to a local maximum.

From the last argument, the skeleton can be seen as the ensemble of pairs of stable fields lines departing from saddle points and connecting them to local maxima. The skeleton field lines can thus be drawn by going along the trajectory with the following motion equation

$$\frac{d\mathbf{r}}{dt} \equiv \mathbf{v} = \nabla \rho, \quad (1)$$

starting from the saddle points, and with initial velocity parallel to the major axis of the local curvature (i.e. parallel to the eigenvector of the Hessian corresponding to λ_1). Trajectory is followed until convergence to a local maximum. This procedure was actually used to draw the skeleton, as explained in details in Appendix.

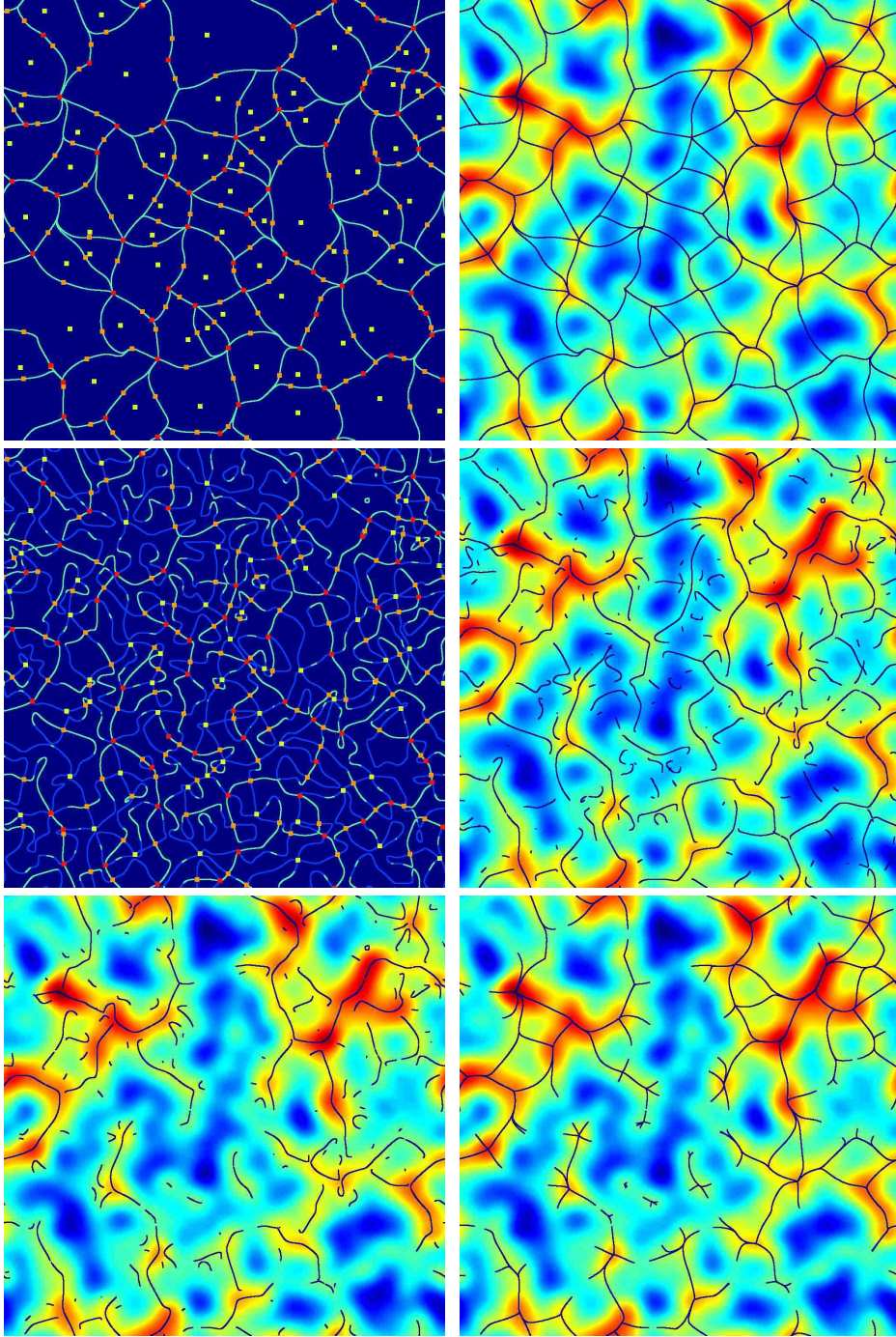


Figure 2. Skeleton and its local approximation for the Gaussian field of Fig. 1.

Upper left panel: the skeleton is drawn as well as the critical points: local minima in yellow, saddle points in orange and local maxima in red. As discussed in the text, the skeleton passes through all the maxima and the saddle points. The local maxima are the nodes where several lines converge, while the saddle points have only one line passing through. Note as well that local maxima are always connected to saddles and reciprocally, except in e.g. the lower left of the panel, when one can see three saddles connected to each other. This configuration is theoretically forbidden unless there is some degeneracy in the field, that we suspect is due to our numerical implementation, as further discussed in Appendix.

Upper right panel: the skeleton is superposed to the smoothed field.

Middle left panel: same as for the upper left panel, but for the local approximation of the skeleton. The dark plus light blue lines assume $S = 0$ [eq. (8)], while the light blue lines verify the more constraining conditions given by eqs. (2) and (3).

Middle right panel: same as upper right panel but for the local approximation of the skeleton.

Lower left and lower right panels: the local approximation and the real skeleton are again superposed to the smooth field, but restricted to over-dense regions $\rho \geq \langle \rho \rangle$.

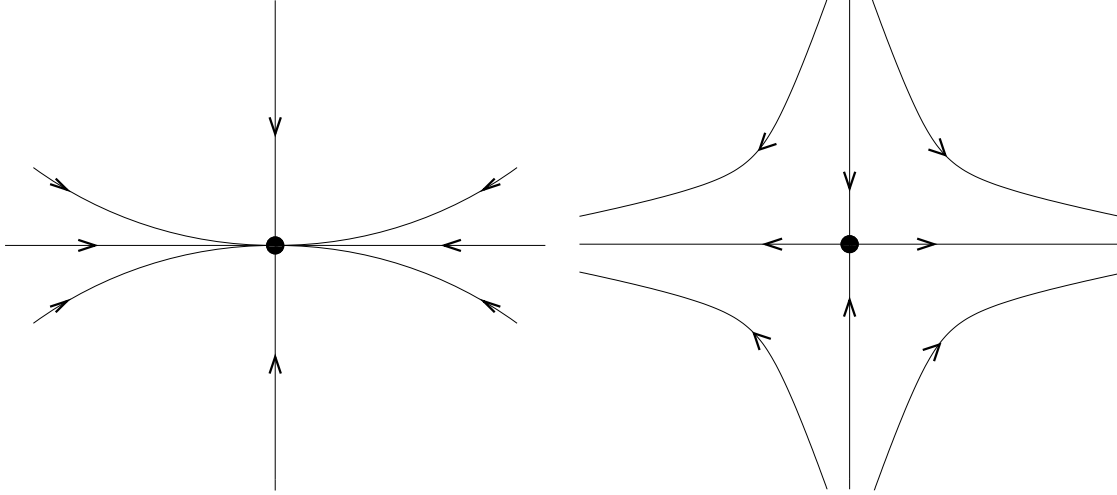


Figure 3. Topology in the neighborhood of critical points (inspired from Jost 2002).

Left panel: expected topology of field lines nearby a maximum, if $\lambda_1 > \lambda_2$. Except for two vertical field lines along the eigenvector corresponding to the smallest eigenvalue, λ_2 , all the lines converging to the node tend to be aligned with the horizontal axis, corresponding to λ_1 . If $\lambda_1 = \lambda_2$, we would face a degenerate situation where all the directions are equivalent.

Right panel: expected topology of field lines nearby a saddle point, if $\lambda_1 > 0 > \lambda_2$. There are only four field lines connected to this point, aligned with the two eigenvectors. The two vertical field lines, corresponding to λ_2 , are unstable since all the other field lines are diverging away from them. Reversely, the two horizontal lines corresponding to λ_1 are stable lines.

2.2 Local approximation

As discussed in Appendix, equation of motion (1) is not easy to solve in practice, even for a smooth field sampled on a finite but thin grid. Furthermore, analytic predictions are very difficult since eq. (1) is non local. This motivates the need for an approximation of the real skeleton with a *local* criterion on the density field and its derivatives of various orders. We shall do so by two means, the first using a more mathematical approach, the second using a more physical approach.

The mathematically motivated derivation consists in Taylor expanding the field around its saddle points and its local maxima. On the skeleton nearby these points, we clearly have, at leading order (and except for degenerate cases)

$$\lambda_2 < 0, \quad (2)$$

$$\mathcal{H} \nabla \rho = \lambda_1 \nabla \rho. \quad (3)$$

This entails a natural definition for the *local* skeleton: it consists of any point of space where eqs. (2) and (3) are verified.

The physically motivated approach consists in considering the field as a landscape, where the third coordinate, r_3 , is given by $r_3 = \rho(r_1, r_2)$. In that case, the isocontour lines of the density field are natural objects for the analyses. Let us consider two pieces of isocontour lines A and B very close to each other and let us move from A to B , following the gradient. We expect the skeleton to take either the short possible or the longest possible path between A and B . Since the path length is inversely proportional to the magnitude of the gradient, the points of interest are those where $|\nabla \rho|$ is locally an extremum along the isocontour.^{||}

^{||} An accurate examination of the neighborhood of local max-

This translates mathematically as follows. If we denote s a curvilinear coordinate along an isocontour, $(r_1(s), r_2(s))$, we have by definition,

$$\frac{\partial \rho}{\partial r_1} \frac{dr_1}{ds} + \frac{\partial \rho}{\partial r_2} \frac{dr_2}{ds} = 0, \quad (4)$$

with the normalization

$$\left(\frac{dr_1}{ds}\right)^2 + \left(\frac{dr_2}{ds}\right)^2 = 1. \quad (5)$$

The gradient is locally an extremum along the isocontour if

$$\frac{d}{dt} (|\nabla \rho|^2) = 0, \quad (6)$$

which gives, using eq. (4),

$$\begin{aligned} \mathcal{S} &\equiv \frac{\partial \rho}{\partial r_1} \frac{\partial \rho}{\partial r_2} \left(\frac{\partial^2 \rho}{\partial r_1^2} - \frac{\partial^2 \rho}{\partial r_2^2} \right) \\ &+ \frac{\partial^2 \rho}{\partial r_1 \partial r_2} \left(\left[\frac{\partial \rho}{\partial r_2} \right]^2 - \left[\frac{\partial \rho}{\partial r_1} \right]^2 \right) = 0. \end{aligned} \quad (7)$$

In fact, it is fairly easy to rewrite this equation as

$$\mathcal{S} = \det(\mathcal{H} \nabla \rho, \nabla \rho) = 0. \quad (8)$$

Therefore, the condition $\mathcal{S} = 0$ is equivalent to say that the gradient is an eigenvector of the Hessian.

However, there is a supplementary condition which

ima and saddle points suggests that the skeleton should take the longest possible way, which in fact implies that the magnitude of the gradient is a local *minimum* along the contour line. However, enforcing such a condition would lead us to examine expressions involving third derivatives of the density field, in disagreement with a leading order approach. Instead, we are going to use less realistic but simpler criteria on the local curvature of the isocontour lines nearby the extrema of the density gradient magnitude to select the points of interest.

comes out naturally: while walking from one field line to another, one prefers to stay on a ridge, that is on the points where the curvature of the isocontour is positive, i.e.

$$\mathcal{C} \equiv \frac{\nabla\rho}{|\nabla\rho|} \cdot \frac{d^2\mathbf{r}}{ds^2} > 0, \quad (9)$$

which translates in, after some algebra based on eqs. (4) and (5),

$$\mathcal{C} = -\frac{1}{|\nabla\rho|^3} {}^t\nabla\rho_{\perp} \mathcal{H} \nabla\rho_{\perp} > 0, \quad (10)$$

where $\nabla\rho_{\perp} \equiv (\partial\rho/\partial r_2, -\partial\rho/\partial r_1)$. So, we have to select among the points verifying eq. (8) those which have $\mathcal{C} > 0$. Since, $\nabla\rho$ is an eigenvector of \mathcal{H} , so is $\nabla\rho_{\perp}$, therefore

$$\mathcal{C} = -\frac{\lambda_2}{|\nabla\rho|} \text{ or } -\frac{\lambda_1}{|\nabla\rho|}. \quad (11)$$

After a simple examination of the various cases, $\lambda_1 \geq \lambda_2 > 0$, $\lambda_1 > 0 > \lambda_2$ and $0 > \lambda_1 \geq \lambda_2$, we finally obviously converge again to eqs. (2) and (3), except for hills, $0 > \lambda_1 \geq \lambda_2$, where equation (10) allows the gradient to be aligned with both axes of the curvature. In this last case, we can see however that the situation $\mathcal{H}\nabla\rho = \lambda_2\nabla\rho$ contradicts the “natural” definition of a ridge. Such a ridge would indeed be more curved along its path than orthogonally to it, a situation clearly unrealistic in the neighborhood of a local maximum.

2.3 Examples

We now compare the local and real skeleton by visual inspection of Figs. 2 and 4, which respectively correspond to a Gaussian realization and its Zel’dovich mapping. We also measure the length of the skeletons as a function of threshold for these two particular examples.

Clearly the local skeleton is an excellent approximation of the real one. Indeed most of the large scale features are very well captured, particularly in the vicinity of maxima and saddle points, as a result of our perturbative approach. In agreement with intuition, the more filamentary is the field, the better is the agreement: the local skeleton seems to perform better in the Zel’dovich map than in the Gaussian one. However, connectivity of the local skeleton is not ensured, at variance with the real one. Furthermore, there are little spurious structures in void patches that do not match any line of the real skeleton. By restricting the comparison to over-dense regions, a large number of these structure disappear and the agreement improves significantly, at least visually.

A more quantitative analysis can be conducted by comparing the measured length of the real and local skeletons in regions where the density exceeds a given threshold, as illustrated by Fig. 5. Contrary to what would suggest the visual inspection of Figs. 2 and 4, the local skeleton is systematically slightly shorter than the real one. The total lengths differ by about 20 percents, both for the Gaussian smooth field and its Zel’dovich mapping. However, as illustrated by left panel of Fig. 3, skeleton field lines converging to a local maximum tend to superpose along the major axis of the local curvature, which produces multiple lines. This feature inherent to the Lagrangian nature of the real skeleton is

missing in the local skeleton, due to its local, Eulerian nature (see also Appendix). Hence, it is not surprising that the local skeleton is shorter than the real one.

3 LINK TO STATISTICS

In this section we focus on the local skeleton. For the sake of simplicity, we study from now on the *total* local skeleton, defined as *the full set of points satisfying the condition $\mathcal{S} = 0$* [eq. (8)]. We first examine the Gaussian case in § 3.1, where specific analytic results are derived and then confronted to numerical experiments. The normalized differential length of the skeleton as a function of density threshold is seen to be very close to the probability distribution function (pdf) of the smoothed field, i.e. a Gaussian.

We thus consider in section § 3.2 some examples of non-Gaussian fields, namely χ^2 distributions with n degrees of freedom, the Zel’dovich mapping discussed previously and, finally, an extreme case where the density contrast is locally enhanced along lines with random orientations. In all these cases, we find again that the differential length of the skeleton scales very much like the pdf, with slightly worse noise properties as expected since this estimator relies on derivatives of the field. This intriguing result, despite its mathematical beauty, might look discouraging for using the skeleton as a test of non-gaussianity. However, our analysis does not use the supplementary information provided by the skeleton, namely its total length, which is considered here as an arbitrary normalization.

3.1 The Gaussian case

In this section, after defining a set of useful notations (§3.1.1), we compute a general expression for the differential length of the skeleton, f , as a function of density threshold (§3.1.2). Then we concentrate on the Gaussian case (§3.1.3) and show that the shape of f depends only on a single spectral parameter, γ , defined below. We demonstrate that for $\gamma = 0$, f is exactly given by a Gaussian. Given the level of complexity of the calculations, we are however lead to rely on a power expansion in γ around a Gaussian to examine the case $\gamma > 0$. This power expansion is checked carefully against numerical experiments (§3.1.4), which indeed show that f deviates only weakly from a Gaussian.

3.1.1 Spectral parameters and dimensionless variables

From now on, we assume without loss of generality that the random smoothed field, ρ has zero average $\langle\rho\rangle = 0$. For convenience we define the following spectral parameters:

$$\sigma_0^2 = \langle\rho^2\rangle, \quad (12)$$

$$\sigma_1^2 = 2\langle\rho_1^2\rangle = 2\langle\rho_2^2\rangle, \quad (13)$$

$$\sigma_2^2 = \frac{8}{3}\langle\rho_{11}^2\rangle = \frac{8}{3}\langle\rho_{22}^2\rangle = 8\langle\rho_{22}^2\rangle, \quad (14)$$

$$\sigma_3^2 = \frac{16}{5}\langle\rho_{111}^2\rangle = \frac{16}{5}\langle\rho_{222}^2\rangle = 16\langle\rho_{112}^2\rangle = 16\langle\rho_{122}^2\rangle, \quad (15)$$

$$\tilde{\gamma} = \sigma_1^2/(\sigma_0\sigma_2), \quad (16)$$

$$\tilde{\gamma} = \sigma_2^2/(\sigma_1\sigma_3), \quad (17)$$

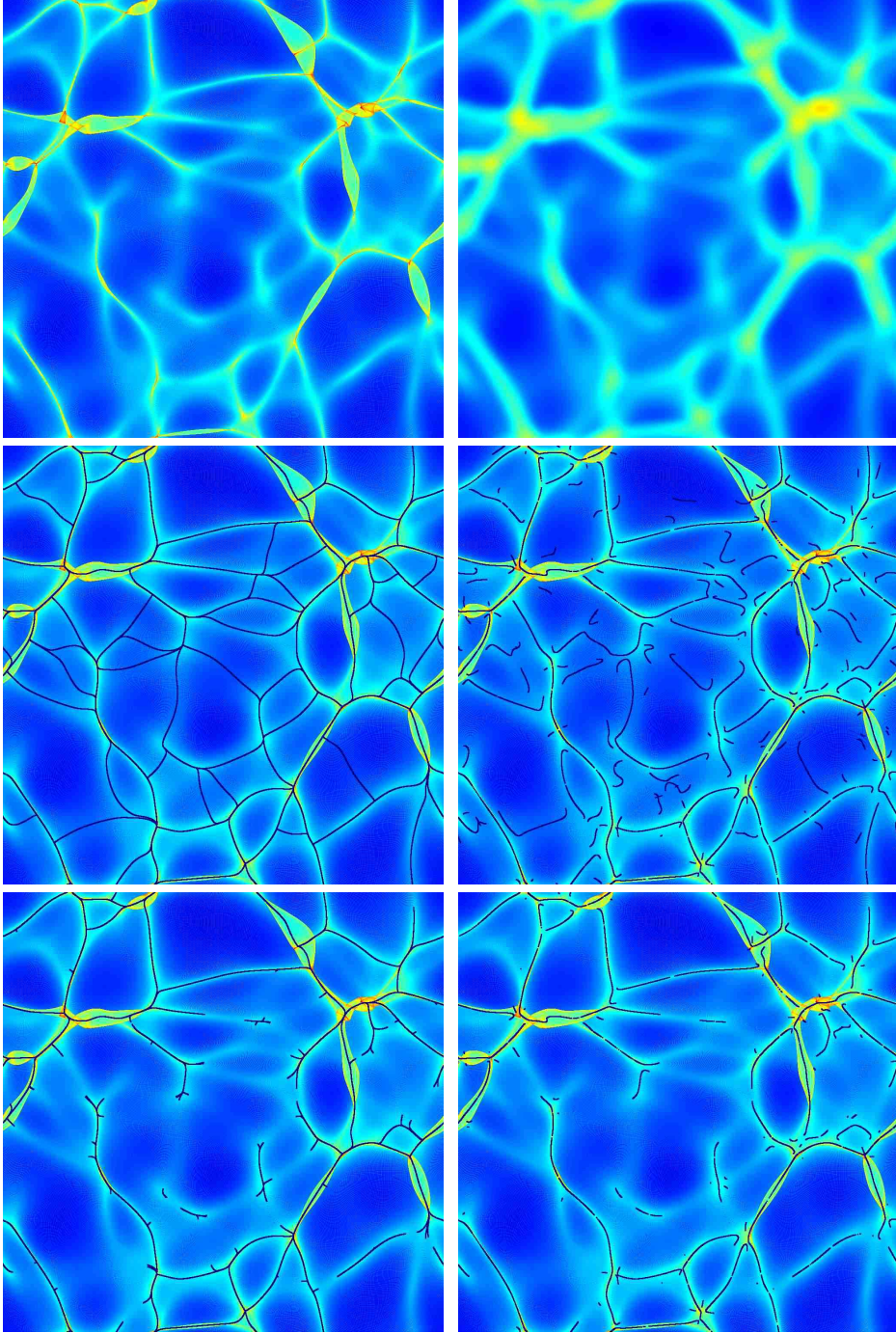


Figure 4. Skeleton and its local approximation for the Zel'dovich mapping of the smoothed Gaussian field of Fig. 1.

Upper left panel: Zel'dovich mapping of the smoothed field: the Lagrangian displacement field \mathbf{P} was normalized so that $\nabla \cdot \mathbf{P} = -(\rho - \langle \rho \rangle) / \sigma \langle \rho \rangle$, where σ^2 is the variance of the initial smooth map.

Upper right panel: the field of the top left panel smoothed with a Gaussian window of radius 12.5 pixels. Such smoothing is necessary to get rid of caustics and to enforce the differentiability required to measure the skeleton. The smoothing scale is such that the large scale features outside caustics are preserved: it has to be small compared to the initial smoothing radius of 25 pixels and large enough compared to the pixel size.

Middle left and middle right panels: respectively, the real and the local skeleton superposed to the Zel'dovich map.

Lower left and lower right panels: respectively, the real and the local skeleton superposed to the Zel'dovich map, but restricted to over-dense regions.

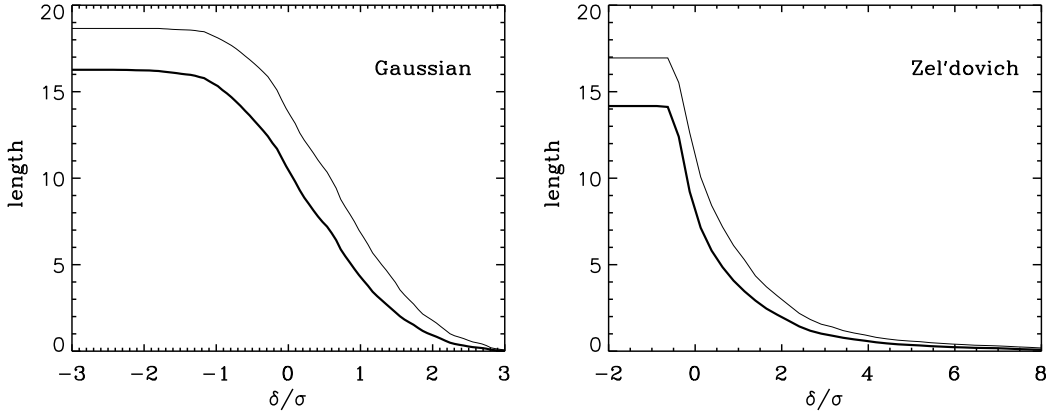


Figure 5. Real versus local skeleton length comparison.

Left panel: the skeleton length in units of sample box length as a function of density threshold, measured for the real (thin curve) and the local (thick curve) skeleton in the smooth Gaussian field of Fig. 1. $\delta/\sigma \equiv (\rho - \langle \rho \rangle)/\sigma(\rho)$ is the density contrast in units of the variance of the smoothed field.

Right panel: same as left panel but for the smoothed Zel'dovich map (top right panel of Fig. 4).

where $\rho_i \equiv \partial\rho/\partial r_i$, $\rho_{ij} \equiv \partial^2\rho/\partial r_i\partial r_j$ and $\rho_{ijk} \equiv \partial^3\rho/\partial r_i\partial r_j\partial r_k$ ($i, j, k = 1, 2$) are its gradient, hessian and matrix of third derivatives, respectively. Using these parameters one can consider the 10 following dimensionless variables:

$$x = \frac{\rho}{\sigma_0}, \quad x_i = \frac{\rho_i}{\sigma_1}, \quad x_{ij} = \frac{\rho_{ij}}{\sigma_2}, \quad x_{ijk} = \frac{\rho_{ijk}}{\sigma_3}, \quad (18)$$

and the dimensionless function $s = \mathcal{S}/(\sigma_1^2\sigma_2)$. That is, according to eq. (7):

$$s = x_1x_2(x_{11} - x_{22}) + x_{12}(x_2^2 - x_1^2). \quad (19)$$

Thus, the points of the random field where the first and second derivatives satisfy the condition $s = 0$ define the total local skeleton. Finally, the derivatives

$$s_i = \mathcal{S}_i/(\sigma_1^2\sigma_3) \quad (20)$$

will also be useful. It is worth noting here that s_i depends on $\tilde{\gamma}$, but not on γ , i.e. $s_i = s_i(x_i, x_{ij}, x_{ijk}, \tilde{\gamma})$.

3.1.2 Length of the skeleton: general expressions

If we denote $\mathcal{P}_s(\rho, \mathcal{S}, \mathcal{S}_1, \mathcal{S}_2)$ the joint probability distribution of the variables ρ , \mathcal{S} , and \mathcal{S}_i for $i = 1, 2$, the expected average of the skeleton length $\mathcal{L}(\rho_{\text{th}})$ per unit area above some threshold ρ_{th} can be derived the following way.

Let us consider a straight line along the direction r_1 and which intersects the isocontour lines, $\mathcal{S} = 0$, at some point, where $\rho > \rho_{\text{th}}$. In the vicinity of such a point, where $\mathcal{S} = 0$ and $d\mathcal{S} = \mathcal{S}_1 dr_1$, we can integrate $\mathcal{P}_s d\rho d\mathcal{S} d\mathcal{S}_1 d\mathcal{S}_2$ over dr_1 from $-dr_1/2$ to $dr_1/2$ and we get, obviously:

$$\int_{r_1 \in [-dr_1/2, dr_1/2], \rho > \rho_{\text{th}}} d\mathcal{S} d\mathcal{S}_1 d\mathcal{S}_2 d\rho \mathcal{P}_s(\rho, 0, \mathcal{S}_1, \mathcal{S}_2) = \int_{\rho > \rho_{\text{th}}} dr_1 \int |\mathcal{S}_1| d\mathcal{S}_1 d\mathcal{S}_2 d\rho \mathcal{P}_s(\rho, 0, \mathcal{S}_1, \mathcal{S}_2). \quad (21)$$

This integral represents the probability to find the point $\mathcal{S} = 0$ along the line $r_2 = \text{const}$ in the range $[r_1 - dr_1/2, r_1 +$

$dr_1/2]$. Note that the absolute value of \mathcal{S}_1 is here necessary since we want to take into account both up-crossing and down-crossing points. Then, the elementary length of the isocontour line $\mathcal{S} = 0$ inside the square $[r_1 - dr_1/2, r_1 + dr_1/2; r_2 - dr_2/2, r_2 + dr_2/2]$ is $dr_2/\cos(\alpha)$, where α is the angle between r_2 and the isocontour line. Since $\cos(\alpha) = |\mathcal{S}_1|/\sqrt{\mathcal{S}_1^2 + \mathcal{S}_2^2}$, using eq. (21) one gets

$$\mathcal{L}(\rho_{\text{th}}) dr_1 dr_2 = \int_{\rho > \rho_{\text{th}}} dr_1 dr_2 \int d\rho d\mathcal{S}_1 d\mathcal{S}_2 \sqrt{\mathcal{S}_1^2 + \mathcal{S}_2^2} \mathcal{P}_s(\rho, 0, \mathcal{S}_1, \mathcal{S}_2). \quad (22)$$

This equation represents the average length of the skeleton per element of area $dr_1 dr_2$. In terms of dimensionless variables, it rewrites

$$\mathcal{L}(x_{\text{th}}) = \int_{x > x_{\text{th}}} dx ds_1 ds_2 \frac{\sigma_3}{\sigma_2} \sqrt{s_1^2 + s_2^2} \mathcal{P}_s(x, 0, s_1, s_2). \quad (23)$$

We shall now look for an analytical expression for this function \mathcal{L} in the case of a Gaussian field.

3.1.3 Towards an analytic expression for a Gaussian field

Deriving eq. (23) we did not consider any special features of the joint probability function \mathcal{P}_s , thus this equation is true for any random field. Unfortunately the derivation of function \mathcal{P}_s is not easy, even in the Gaussian case, that we examine now.

We consider the 10 components random vector, \mathbf{a} ,

$$\mathbf{a} = (x, x_i, x_{ij}, x_{ijk}) \quad (i, j, k = 1, 2), \quad (24)$$

and the probability distribution function $\mathcal{P}(\mathbf{a})$. In the Gaussian case, this can be written as

$$\mathcal{P}(\mathbf{a}) = \frac{1}{[(2\pi)^{10} |\mathbf{M}|]^{-\frac{1}{2}}} \exp\left[-\frac{1}{2} \mathbf{a} \mathbf{M}^{-1} \mathbf{a}^T\right] \quad (25)$$

where \mathbf{M} is the covariance matrix, $\mathbf{M} = \langle \mathbf{a} \mathbf{a}^T \rangle$, and $|\mathbf{M}|$ its determinant. Then, eq. (23) can be rewritten using $\mathcal{P}(\mathbf{a})$

$$\mathcal{L}(x_{\text{th}}) = \int_{x > x_{\text{th}}, s=0} \frac{\sigma_3}{\sigma_2} \sqrt{s_1^2 + s_2^2} \mathcal{P}(\mathbf{a}) d\mathbf{a}. \quad (26)$$

For further investigation, it is particularly convenient to consider the following variables:

$$q = x_{11} - x_{22}, \quad u = 2x_{12}, \quad v = x_{11} + x_{22}. \quad (27)$$

We are interested in the distribution of the skeleton length over just one variable x_{th} . It is worth mentioning that using the variables defined in eq. (27), x correlates only with v and does not correlate with either q , u , x_i nor x_{ijk} , i.e.

$$\langle xq \rangle = \langle xu \rangle = \langle xx_i \rangle = \langle xx_{ijk} \rangle = 0, \quad (28)$$

$$\langle xv \rangle = -\gamma. \quad (29)$$

Taking into account eqs. (27) and (29), one can represent $\mathcal{P}(\mathbf{a})$ in the following way:

$$\mathcal{P}(\mathbf{a}) = \frac{1}{\sqrt{1-\gamma^2}} \exp\left[-\frac{(x+\gamma v)^2}{2(1-\gamma^2)}\right] \tilde{\mathcal{P}}(x_i, q, u, v, x_{ijk}). \quad (30)$$

In order to take into account the condition $s = 0$ in eq. (26), we should perform one more substitution:

$$x_1 = r \cos(\varphi), \quad x_2 = r \sin(\varphi), \quad (31)$$

$$q = p \cos(2\psi), \quad u = p \sin(2\psi). \quad (32)$$

It is easy to see that with these new variables, the function s in eq. (19) reads:

$$s = \frac{1}{2} p r^2 \sin[2(\varphi - \psi)]. \quad (33)$$

The condition $s = 0$ is now transformed into a simple relation between the angles φ and ψ . The length of the skeleton can therefore be written as follows:

$$\mathcal{L}(x_{\text{th}}) = \frac{\sigma_3}{\sigma_2} \int_{x_{\text{th}}}^{\infty} dx \int_{-\infty}^{\infty} dv \frac{e^{-\frac{(x+\gamma v)^2}{2(1-\gamma^2)}}}{\sqrt{1-\gamma^2}} \int d\Omega \sqrt{s_1^2 + s_2^2} \times$$

$$[\delta_{\text{D}}(\varphi - \psi) + \delta_{\text{D}}(\varphi - \psi + \pi/2)] \hat{\mathcal{P}}(r, p, \varphi, \psi, x_{ijk}, v) \quad (34)$$

where $d\Omega = p dp r dr dx_{ijk} d\psi d\varphi$ and δ_{D} is the usual delta function. This equation will give us the total length of the skeleton \mathcal{L}_{tot} if we consider $x_{\text{th}} \rightarrow -\infty$. From eqs. (19) and (34) one can see that the differential length normalized by the total length is:

$$f \equiv -\frac{1}{\mathcal{L}_{\text{tot}}} \frac{\partial \mathcal{L}}{\partial x} = \int_{-\infty}^{+\infty} dv \mathcal{C}(v) \frac{e^{-\frac{(x+\gamma v)^2}{2(1-\gamma^2)}}}{\sqrt{1-\gamma^2}}. \quad (35)$$

Therefore, remarkably, f is a function of x and only one spectral parameter γ . The quantity $f(x, \gamma) dx$ simply represents the fraction of the skeleton length between the levels x and $x + dx$. However, the unknown function $\mathcal{C}(v)$ is rather cumbersome to estimate analytically. We examine in next section a way to avoid its calculation, but which relies partly on numerical experiments.

3.1.4 Final expression in the case of a Gaussian field

The first thing to notice, when examining eq. (35), is that in the limit $\gamma = 0$, f is exactly a Gaussian:

$$f(x, \gamma = 0) = \frac{1}{\sqrt{2\pi}} e^{-x^2/2}. \quad (36)$$

We thus expect f to depart only weakly from a Gaussian if γ is small enough, which motivates for a power-expansion of $f(x, \gamma)$ in γ around a Gaussian.

According to eq. (35), $f(x, \gamma)$ satisfies the following partial differential equation:

$$\frac{\partial f}{\partial \gamma} \gamma = -\frac{\partial}{\partial x} \left(\frac{\partial f}{\partial x} + x f \right). \quad (37)$$

Since $f(x, \gamma)$ is a probability distribution function, it should satisfy the following condition:

$$\int f(x, \gamma) dx = 1. \quad (38)$$

To try to solve eq. (37), we examine solutions of the form

$$f(x, \gamma) = \left\{ \sum_{n \geq 0} g_n(x) \gamma^n \right\} \frac{1}{\sqrt{2\pi}} e^{-x^2/2}. \quad (39)$$

Injecting this expression in eq. (38) leads to

$$\frac{d^2 g_n}{dx^2} - x \frac{dg_n}{dx} + n g_n = 0. \quad (40)$$

Setting $y = x/\sqrt{2}$, we find

$$\frac{d^2 g_n}{dy^2} - 2y \frac{dg_n}{dy} + 2n g_n = 0, \quad (41)$$

a differential equation followed by Hermite polynomials, $H_n(y)$. A more detailed examination of the possible solutions gives

$$g_n(x) = H_n(x) \left[C_n + D_n \int^{x/\sqrt{2}} dy \exp(y^2)/H_n^2(y) \right]. \quad (42)$$

Questionable arguments based on enforcing the convergence of the moments of f with respect to x suggest $D_n = 0$. Symmetry of the Gaussian field with respect to $x = 0$ implies $C_{2n+1} = 0$. As a result we expect f to have the following form

$$f(x, \gamma) = \left\{ \sum_{n \geq 0} C_{2n} H_{2n}(x/\sqrt{2}) \gamma^{2n} \right\} \frac{1}{\sqrt{2\pi}} e^{-x^2/2}. \quad (43)$$

with $C_0 = 1$, from normalization (38). Note that this expression is nothing but a Gram-Charlier expansion prior to standardization [see Stuart & Ord 1994, eq. (6.32)]. It can be valid in practice only if the departure from a Gaussian is weak. Alternatively, thus, we could have derived eq. (43) by trying to find solutions of the form

$$f(x, \gamma) = \left\{ \sum_{n \geq 0} h_{2n}(\gamma) H_{2n}(x/\sqrt{2}) \right\} \frac{1}{\sqrt{2\pi}} e^{-x^2/2}, \quad (44)$$

using directly the Gram-Charlier expansion.

The coefficients C_{2n} , $n \geq 1$, remain to be determined. We therefore performed a set of numerical experiments which was used as well to test extensively our skeleton analysis software (see discussion in Appendix). We generated scale-free random Gaussian fields with power-spectra $P(k) \propto k^n$, $n = 0, -1$, and -2 ($\gamma = 0.71, 0.58, 0.32$, respectively). For each value of n we performed 100 realizations over a periodic grid of size 1024×1024 pixels (except for $n = 0$, where we used 2048×2048 pixels). The field was smoothed with a window of radius 5 pixels (10 pixels for

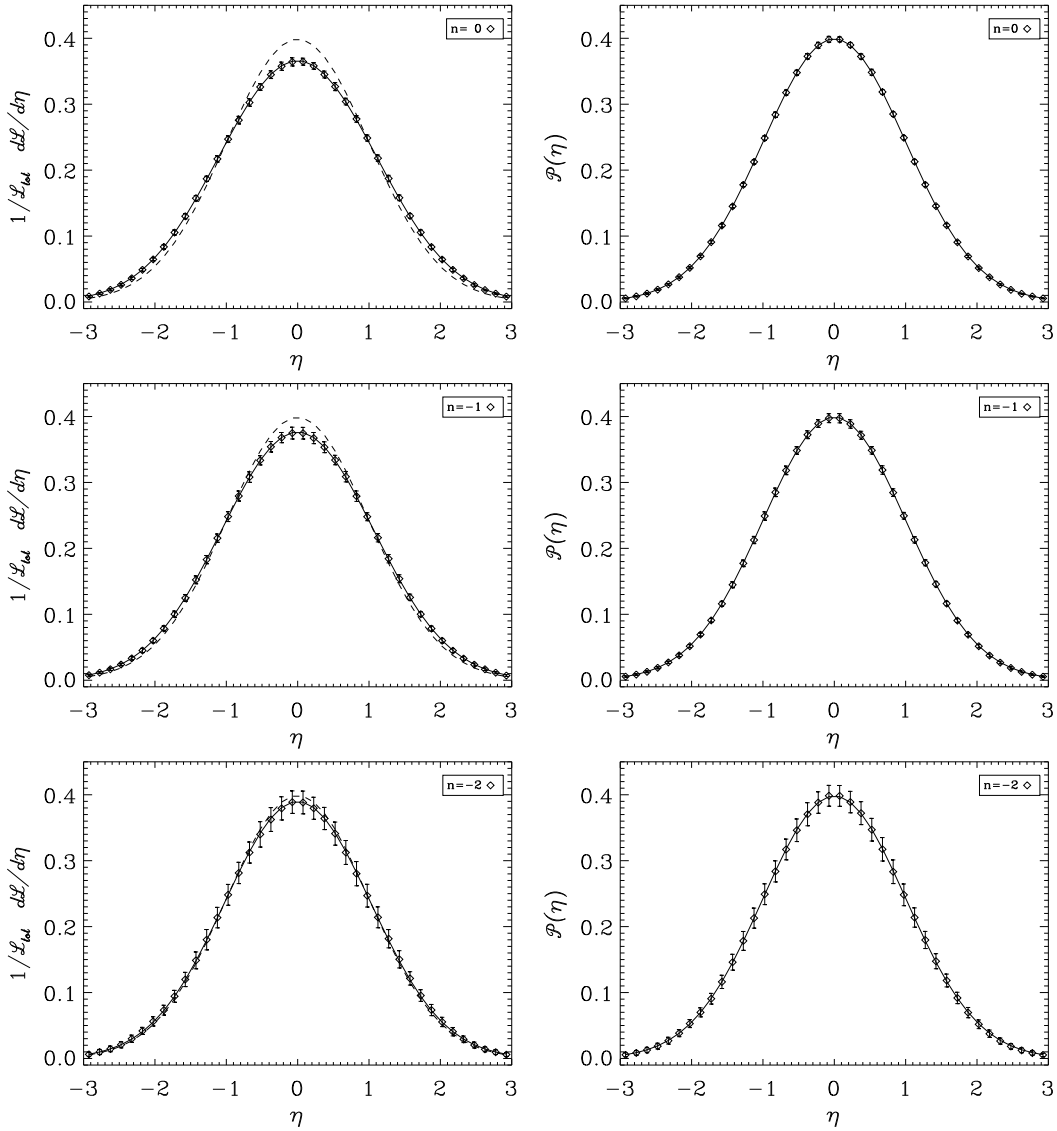


Figure 6. The measured differential length of the total local skeleton [eq. (8), left panels] and the pdf of the smoothed field for scale-free Gaussian random fields (right panels) with power-spectra $P(k) \propto k^n$, $n = 0, -1$ and -2 as indicated on each panel, as functions of normalized density contrast, $\eta = \delta/\sigma = x = \rho/\sigma$. For each value of n , 100 realizations were performed on a periodic grid of size 1024×1024 pixels (2048×2048 for $n = 0$), and then smoothed with a Gaussian window of radius 5 pixels (10 pixels for $n = 0$). On left panels, the dashed and solid curves correspond respectively to the Gaussian limit and our semi-analytic expression (47). On right panels, the solid curves correspond to the Gaussian limit. The symbols with errorbars are the measurements.

$n=0$).^{**} The results are shown in Figure 6 for the differential skeleton length (left panels) and for the measured pdf (right panels). The errorbars are obtained by the scatter over the 100 realizations. They are of the same order for the skeleton as for the pdf, although slightly larger for the former than for the latter. These small differences will be more visible and explained in the next section, which deals with non Gaussian cases.

^{**} The case $n = 0$ requires a larger smoothing window, compared to the pixel size, see discussion in Appendix. 10 pixels is a rather conservative but safe choice for $n = 0$. It implies to use images of 2048×2048 pixels, in order to preserve the ratio between the size of the smoothing window and the total size of the image, chosen for all values of n to be approximately equal to $1/200$.

We see that the departure of $f(x, \gamma)$ from a Gaussian (dotted curve on all the panels) is quite weak, even for $n = 0$, which corresponds to a large value of $\gamma = 0.71$. As a result, only first order correction is needed, and we find numerically that

$$C_0 = 1, \quad C_2 = 0.17, \quad (45)$$

$$C_{2n} = 0 \quad \text{for } n > 2, \quad (46)$$

provides an excellent approximation to $f(x, \gamma)$ in the Gaussian limit (solid curve on each left panel). Our final expression for the normalized differential length of the total local skeleton, is thus, for a smoothed Gaussian field:

$$f(x, \gamma) = \frac{1}{\mathcal{L}_{tot}} \frac{\partial \mathcal{L}}{\partial x} \simeq \frac{1}{\sqrt{2\pi}} e^{-x^2/2} [1 + 0.17 \gamma^2 (1 - x^2)]. \quad (47)$$

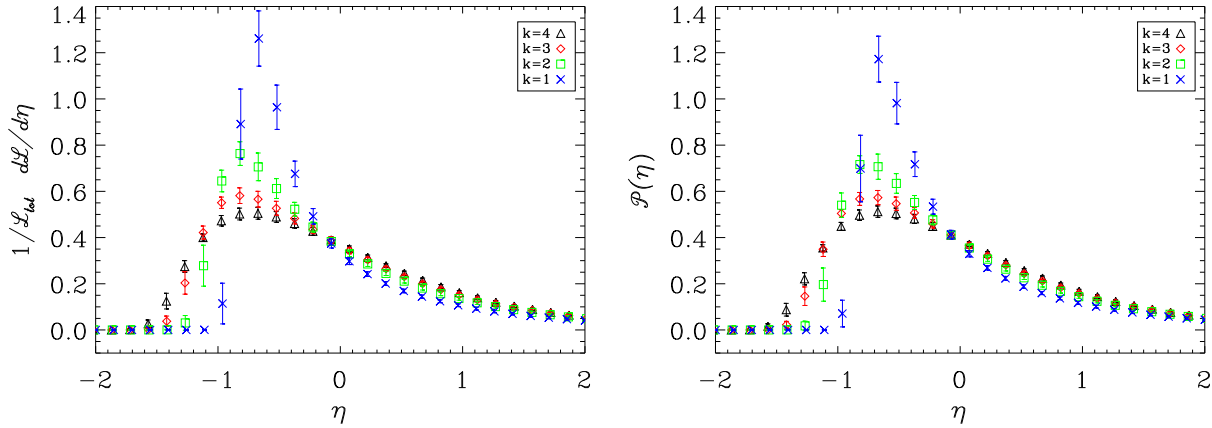


Figure 7. The measured differential length (left panel) of the total local skeleton [eq. (8)] and the pdf of the smoothed field (right panel) for χ^2 distributions with $k = 1, 2, 3$ and 4 degrees of freedom as indicated on the upper right part of each panel.

3.2 The non Gaussian case

We now consider a few non Gaussian experiments. The first one is the case of a χ^2 distribution with k degrees of freedom (using scale-free Gaussian seeding fields with spectral index $n = -2$). Fig. 7 is similar to Fig. 6, but for χ^2 distributions with $k = 1, 2, 3$ and 4 . The number of realizations, the resolution of the maps and the smoothing are the same as in Fig. 6. Clearly, the non Gaussian nature of the field is well reflected by the skeleton. In fact, and quite surprisingly, its differential length again scales very much like the pdf of the smoothed density field: there is very little difference between left and right panels of Fig. 7, except maybe for the size of the errorbars: those are slightly larger for the skeleton than for the pdf, as expected. Indeed, the skeleton construction relies on estimates of derivatives in a one dimensional subset of pixels in the density map, it is therefore more sensitive to noise.

Our second non Gaussian experiment is the Zel'dovich map studied in § 2 (Fig. 4). Figure 8 compares the differential length of the total local skeleton to the measured pdf. Again, for this single realization of a strongly non Gaussian field, the agreement between both measurements is very good, even in the high density tail. Note that the curve for the skeleton is slightly more irregular than the one for the pdf, as expected.

Finally, to confirm the validity of the striking results of this section, we decided to perform a quite extreme test as illustrated by Fig. 9. Taking the field generated on left panel of Fig. 1, we increased locally the density contrast by a factor 1600 along 5 lines 800 pixels long and 1 pixel large, with random positions and random orientations. This map was then smoothed with a Gaussian window of radius 30 pixels, as shown on upper panel of Fig. 9. The total local skeleton obtained from this map is displayed in middle panel. The lines are clearly visible on the picture as comb like structures. As shown in lower panel, the skeleton differential length again scales very much like the pdf.

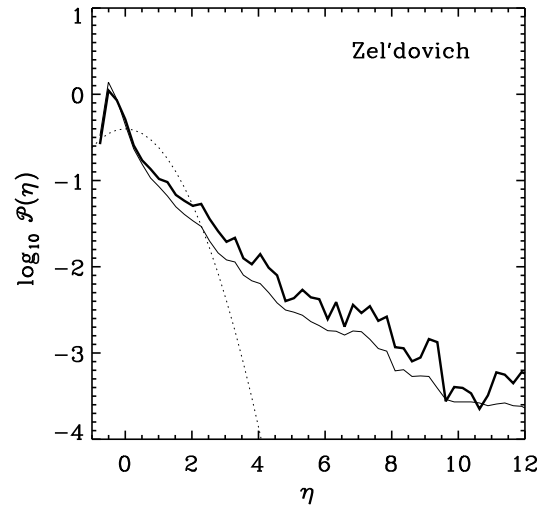


Figure 8. Comparison of differential length of the total local skeleton [points of space verifying eq. (8)] with the pdf of the smoothed density field for the Zel'dovich map of Sect. 2, both as functions of the normalized density contrast $\eta = \delta/\sigma$. The thick/thin curve corresponds to the skeleton/pdf. For reference, the Gaussian limit is also plotted as a dotted curve.

4 DISCUSSION AND LINKS TO DYNAMICS

In this paper, we studied some properties of the skeleton of a 2D random smooth field. This latter is given by an ensemble of special field lines connecting saddle points to extrema. It is aimed to give accurate account of the network of filaments in the field. The skeleton is a nonlocal object, difficult to build with a reliable algorithm and to use to perform analytic calculations. We thus tried to find a local approximation to it, depending on the field and its derivatives. To do that, we used two approaches, a mathematically motivated one based on a Taylor expansion of the field around local maxima and saddle points, and a physically motivated one based on an examination of isocontour lines. They both lead to the same conclusion. After comparing the resulting *local* skeleton to the real one, we performed statistical analyses of its length as a function of density threshold. To simplify the calculations, we considered a larger set of curves than the local skeleton

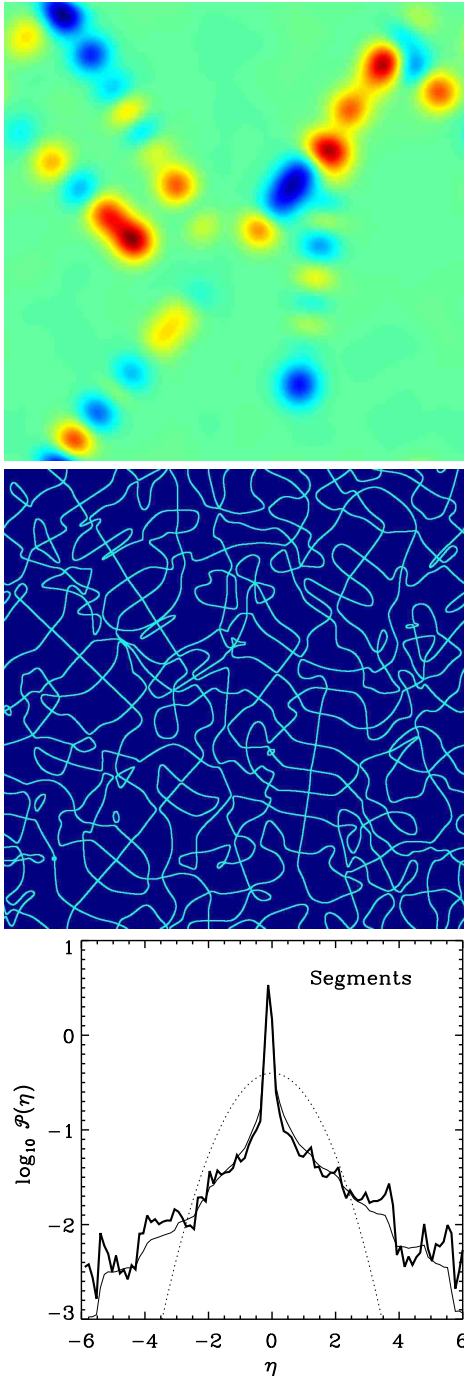


Figure 9. The case of a Gaussian field with lines superposed on it.

Top panel: the Gaussian field of left panel of Fig. 1, where the density contrast has been increased by a factor 1600 along five lines (800 pixels long and one pixel large) randomly located and oriented, then smoothed with a Gaussian window of radius 30 pixels.

Middle panel: the total local skeleton obtained from the smoothed field [points of space verifying eq. (8)].

Bottom panel: the measured skeleton length (thick line) compared to the pdf (thin line) of the smooth density field, as functions of the normalized density contrast $\eta = \delta/\sigma$. The dots correspond to the Gaussian limit. Note that due to our procedure, the field has very strong kurtosis, but no skewness. Note as well that the central peak is a Gaussian with the variance of the initial Gaussian field of right panel of Fig. 1.

but still containing it, that we called the *total* local skeleton. Having initially in mind to use the total local skeleton as a test of non Gaussianity in CMB maps, we compared its differential length as function of the density threshold with the measured probability distribution function (pdf) of the smoothed field. The results of our paper can be summarized as follows:

(i) By definition the real skeleton is the ensemble of pairs of field lines departing from saddle points, aligned initially with the major axis of local curvature (corresponding to the largest eigenvalue of the Hessian) and connecting them to local maxima. These field lines are drawn by going along the trajectories with the equation of motion $dx/dt = \nabla\rho$ until convergence to a local maximum.

(ii) A very good approximation to the real skeleton, the *local* skeleton, is given by points of space where the gradient is aligned with the major axis of local curvature and where the second component of the local curvature is negative (i.e. the smallest eigenvalue of the Hessian is negative). We noticed however that the local skeleton was shorter than the real one, as expected, due to the Lagrangian nature of the latter, which can have more than two fields lines converging to local maxima, at variance with the former.

(iii) The *total* skeleton is given by all the points of space where the gradient is aligned with one axis of the curvature. Its differential length, as a function of density threshold, is seen to scale very closely like the pdf of the smoothed density field. This is explicitly demonstrated in the Gaussian case with analytic calculations.

The result mentioned in last point might be discouraging for using the total local skeleton as a test of non Gaussianity in 2D maps, since it does not do better than the much simpler pdf. Moreover, since the skeleton depends on local derivatives of the density field, it is expected to behave less well than the pdf with respect to the noise, although we did not investigate that in details, except in part for cosmic variance effects. However, our analysis was not exhaustive. There might exist some counterexamples where the skeleton differential length scales differently from the pdf. Our analyses relied on isotropic smoothing with a Gaussian window and we suspect that this contributes to making the skeleton differential length very alike the pdf. More importantly in our analyses, we kept the full skeleton length, $\mathcal{L}(-\infty)$, as an adjustable parameter. In fact, this length does bring significant additional pieces of information and should be taken into account while comparing models predictions to measurements. Its analytical calculation in the Gaussian limit, although theoretically feasible, is rather cumbersome: we left it for future work, having in mind that it can be fairly determined numerically through appropriate realizations of the models.

Along this paper, we did not address dynamics, although we used a Zel'dovich map to illustrate our purpose. The skeleton is in fact a quite useful tool for the analysis of the large scale structure distribution and the understanding of its dynamics. Indeed, recall that we initially defined the skeleton as the border of void patches (§ 2.1) and that the void patches are given by the regions of space containing all the points converging to the same local minimum while going along the field lines in opposite direction to the gradient. One can similarly associate the peak patches to local max-

ima (Bond & Myers 1996a). Together with the skeleton, the peak patches are the building blocks of the observed large scale structures in the Universe.

Indeed, in the standard approach of hierarchical formation of galaxies, the peak patches collapse and merge together at successive times. The merging of peak patches can also be seen as the collapse of larger peak patches constituted by their progenitors. Within a multi-scale approach, these latter can be obtained by smoothing the field at increasing scales, each smoothing scale corresponding to a different collapse time, as illustrated by Fig. 10. This peak patch approach was in fact used extensively by Bond & Myers (1996a,b,c) to produce a simplified but quite accurate description of large structure dynamics, including the evolution of non linear objects from galaxies to clusters of galaxies, their merging history as well as their large scale motions.^{††} Note that peak patches are rather compact, and thus can be well approximated by ellipsoids, lending credence to the Bond & Myers approach. This also stems from a Taylor expansion of the field around local maxima.

This line of thought can be followed further. Indeed, the local maxima are by definition located on the skeleton along which the matter flows: merging of earlier collapsed patches will take place at the nodes of the skeleton (see also caption of Fig. 10). This description is well known and understood through the adhesion approximation (e.g., Kofman & Shandarin 1988; Kofman, Pogosyan & Shandarin 1990).

Note however that the skeleton itself has its own dynamics, as illustrated by Fig. 11: filaments composing it can move and be distorted due to large scale flows, but can also merge together. For the particular example considered here, Fig. 5 shows that the total length of the skeleton is approximately conserved. It is slightly shorter in the Zel'dovich case compared to initial conditions as a result of the competition between merging and stretching.

Since the matter tends to flow along the lines of the skeleton, these latter represent a useful reference frame to study internal structure and dynamics of filaments in the Universe, with well prescribed procedure to define them, given a typical scale length. In practice, this latter should be larger than the size of clusters of galaxies, and smaller than the size of super-clusters, i.e. of order of a few Mpc. In that case, one knows that the skeleton reflects rather well the initial primordial one (Bond, Kofman & Pogosyan 1996). Note again that the skeleton length can be measured in a cosmological volume, and compared to theoretical predictions.

Since we are in the 2D case, the discussion concerning the dynamics remained at the qualitative level. More quantitative analyses in 3D are left for future work.

ACKNOWLEDGMENTS

S.C. and O.D. thanks the Oxford Astrophysics group, where part of this project was conducted, for its hospitality. We also thank J. R. Bond, F. R. Bouchet and D. Pogosyan for useful discussions. The numerical calculations were performed with a dedicated FORTRAN 90 package, *FasToCh*, available on request from the authors and developed as part

of GPH428 submodule of HFI level 2 in the framework of Planck Surveyor preparation. The numerical calculations were performed at IAP on MAGIQUE (Silicon Graphics O3K, 14 processors, 20Gb memory).

REFERENCES

- Aghanim, N., Forni, O., 1999, *A&A* 347, 409
 Bernardeau, F., Colombi, S., Gaztañaga, E., Scoccimarro, R., 2002, *Phys. Rep.* 367, 1
 Babul, A., Starkman, G. D., 1992, *ApJ* 401, 28
 Bardeen, J. M., Bond, J. R., Kaiser, N., Szalay, A. S., 1986, *ApJ* 304, 15
 Barrow, J. D., Bhavsar, S. P., Sonoda, D. H., *MNRAS* 216, 17
 Bertschinger, E., 2001, *ApJS* 137, 1
 Bhavsar, S. P., Barrow, J. D., 1983, *MNRAS* 205, 61P
 Bond, J. R., Efstathiou, G., 1987, *MNRAS* 226, 655
 Bond, J. R., Kofman, L., Pogosyan, D., 1996, *Nature* 380, 603
 Bond, J. R., Myers, S. T., 1996a, *ApJS* 103, 1
 Bond, J. R., Myers, S. T., 1996b, *ApJS* 103, 41
 Bond, J. R., Myers, S. T., 1996c, *ApJS* 103, 63
 Chiang, L.-Y., Coles, P., 2000, *MNRAS* 311, 809
 Colombi, S., Pogosyan, D., Souradeep, T., 2000, *Phys. Rev. Lett.* 85, 5515
 Doré, O., Colombi, S., Bouchet, F. R., 2003, *MNRAS*, in press (astro-ph/0202135)
 Doroshkevich, A. G., 1970, *Astrofizica*, 6, 581 [*Astrophysics* 6, 320]
 Doroshkevich, A. G., Tucker, D. L., Lin, H., Turchaninov, V., Fong, R., 2001, *MNRAS* 322, 369
 Gott, J. R. III, Melott, A. L., Dickinson, M., 1986, *ApJ* 306, 341
 Hobson, M. P., Jones, A. W., Lasenby, A. N., 1999, *MNRAS* 309, 125
 Jost, J., 2002, *Riemannian Geometry and Geometric Analysis* (Springer, third edition)
 Kerscher, M., 2000, *Lecture Notes in Physics* 554, 36
 Kofman, L., Shandarin, S., 1988, *Nature* 334, 129
 Kofman, L., Pogosyan, D., Shandarin, S., 1990, *MNRAS* 242, 200
 Mecke, K. R., Buchert, T., Wagner, H., 1994, *A&A* 288, 697
 Milnor, J., 1963, *Morse Theory* (Princeton University, Princeton, NJ)
 Monaco, P., Theuns, T., Taffoni, G., Governato, F., Quinn, T., Stadel, J., 2002, *ApJ* 564, 8
 Naselsky, P. D., Novikov, D. I., Silk, J., 2002, *ApJ* 565, 655
 Peebles, P. J. E., 1980, *The Large-Scale Structure of the Universe* (Princeton Univ. Press, 1980)
 Phillips, N. G., Kogut, A., 2001, *ApJ* 548, 540
 Press, W. H., Teukolsky, S. A., Vetterling, W., Flannery, B. P., 1992, *Numerical Recipes in FORTRAN. The Art of Scientific Computing* (Cambridge Univ. Press, 1992)
 Sahni, V., Sathyaprakash, B. S., Shandarin, S. F., 1998, *ApJ* 495, L1
 Shandarin, S. F., 1983, *Sov. Astron. Lett.* 9, 104
 Shandarin, S. F., 2002, *MNRAS* 331, 865
 Stuart, A., Ord, J. K., 1994, *Kendall's Advanced Theory of Statistics*, sixth edition, volume I, *Distribution Theory* (Edward Arnold, Halsted Press, New York-Toronto)
 Tomita, H., 1986, *Prog. Theor. Phys.* 75, 482
 Zel'dovich, Ya. B., 1970, *A&A* 5, 84
 Zel'dovich, Ya. B., 1982, *Sov. Astron. Lett.* 8, 102
 Zel'dovich, Ya. B., Einasto, J., Shandarin, S. F., 1982, *Nature* 300, 407

^{††} See also Monaco et al. 2002 for a similar algorithm.

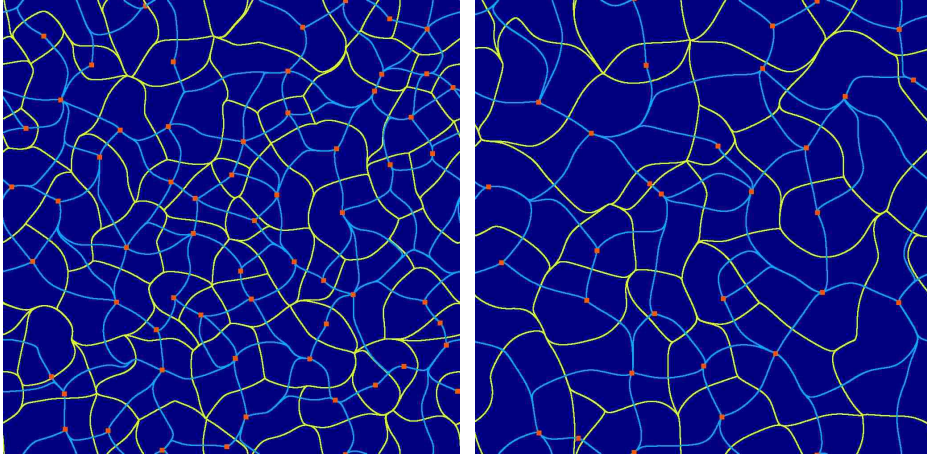


Figure 10. The skeleton and the peak patches for the Gaussian field of Fig. 1, at two different smoothing radii ℓ . The left panel corresponds to $\ell_1 = 25$ pixels, as previously. The right panel corresponds to $\ell_2 = 25\sqrt{2} \simeq 36$ pixels. The skeleton is represented by the blue lines, and the peak patches borders (the dual skeleton) by the golden ones. Each red point corresponds to a local maximum. Left and right panels can be seen as a Lagrangian view of the system at two different times, describing the merging of structures.

Clearly, the peak patches of the right panel can be seen as mergers of peak patches of the left panel, even if mergers can occur differently according to the place of interest: some peak patches survive, i.e. do not merge with others, some of them experience merging with one or more neighbors. As a result, the skeleton of right panel is approximately made of a connected subset of lines composing the skeleton of left panel.

Note that on the lower left corner of left panel, there is a peak patch containing no local maximum. This is clearly an artifact from our numerical approach, which did not detect it. This is not surprising since we noticed earlier (Fig. 2) that something was wrong with the connectivity of the skeleton between critical points in this location.

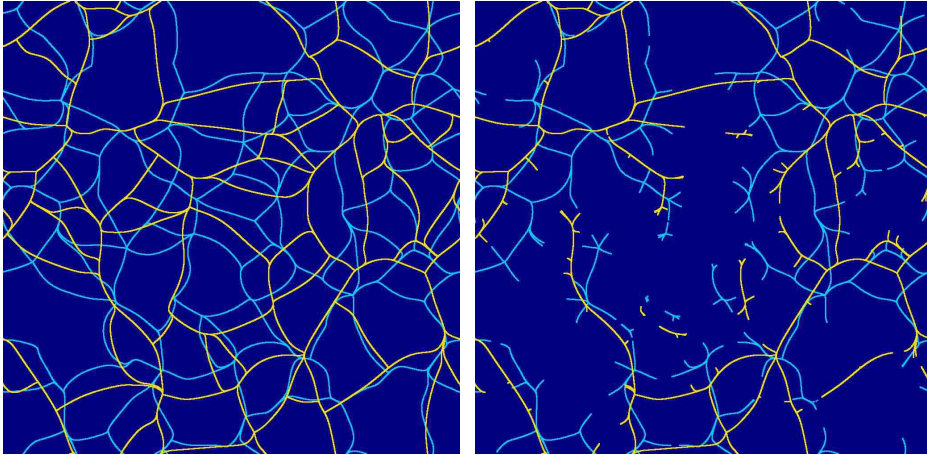


Figure 11. Dynamical evolution of the skeleton for the smooth Gaussian field of Fig. 1.

Left panel: the final skeleton obtained from the Zel'dovich mover (i.e. as explained in Fig. 4, golden lines) superposed to the initial one (blue lines).

Right panel: same as left panel but for over-dense regions.

One can clearly match the details in the initial pattern of filaments to the final one, except for mergers as in e.g. the top right corner and the left side of the panel. Note as well the expansion of the central under-dense region.

APPENDIX A: NUMERICAL APPROACH

The numerical calculations were performed with a dedicated FORTRAN 90 package: FasToCh^{‡‡} (Fast Topological Chase).

While confronting the measurements to the theoretical predictions of Sect. 3.1 for the Gaussian case, we tested ex-

tensively pixelization and finite volume effects by generating maps at various resolutions and smoothed at various scales. We tried as well various schemes described below for computing derivatives and interpolating the field, and we run many different realizations of the same power-spectrum. Finite volume effects are more important for smaller values of the spectral index, n , while pixelization effects, on the contrary, increase with n . In principle if the smoothing length ℓ is very large compared to the pixel size and very small

^{‡‡} Available on request from the authors.

compared to the map size, L , both these effects should be negligible, as we found for $n = 0, -1$ and -2 . Practically, 10 pixels $\lesssim \ell \lesssim L/20$ is generally a safe choice, but in fact the range of available scales depends on the statistics considered as discussed more in detail below on details of the field properties, in particular its power-spectrum shape. We also tested anisotropy effects by generating the initial random field with or without Hanning filtering, the latter insuring isotropy at small scales (e.g. Berstchinger 2001) and found that they were insignificant.

Before entering into the details of the skeleton construction, we first detail the issue of computing reliably the successive derivatives of the field. We examined both Fourier methods and the simplest finite difference schemes. Throughout this paper, we used the Fourier method but the simple finite difference method is both faster and easier to use when the coverage is more intricate such as in galaxy catalogs or in CMB experiments. We also investigated pixelization effects and found that they are negligible provided that the smoothing window is large enough, i.e. a few pixels radius, typically $\ell \gtrsim 3$. However this of course depends on the type of unsmoothed map considered: if there is a lot of small scale power in the map, it is necessary to smooth it more to have reliable estimates of the derivatives.

We also tested bicubic interpolation (e.g. Press et al. 1992) which has the advantage of warranting divergence-free gradient at all positions within a pixel. Practically, this means that given the field values at the pixel centers, as well as pre-computations of the gradient and of the diagonal terms of the Hessian (with either Fourier or finite difference), any quantity can be computed self-consistently at any location within the pixels, including the off-diagonal terms of the Hessian. This property is in principle particularly critical when building the real skeleton. In practice, however, the improvements brought by the bicubic interpolation were insignificant as compared to the simpler and faster bilinear interpolation, which was finally used for all the calculations.

Drawing the local skeleton is simple if one sees that the equation $\mathcal{S} = 0$ [eq. (8)] corresponds to the zero isocontour of the field \mathcal{S} . This can be performed with a standard method as we now explain. Given a square of four neighboring pixels and the corresponding values of \mathcal{S} , we first determine whether the linearly interpolated field cancels along two sides of the square. If this happens, this means that the isocontour curve crosses the square. We locally approximate this curve by a segment which extremities are located on the edges of the square. The coordinates of the segment ends are easily found using dual interpolation. The length of the skeleton is found by adding all the individual segment lengths. There are however particular cases where two pieces of isocontour can intersect at the same point (e.g., at a critical point) or become very close to each other. This can produce configurations where the field cancels on 4 edges of the square. In that case, we cannot compute reliably the length of the isocontour within the square, but the relative contribution of these configurations is increasingly small with the smoothing length. To make these contributions negligible, and to insure as well that the effect of approximating the local skeleton locally by straight lines is negligible, the smoothing length should be of order a few pixels size, typically $\ell \gtrsim 5$ for spectral index $n \lesssim -1$. However, the smoothing radius has to remain small compared to the map size,

in order to avoid finite volume effects, typically $\ell \lesssim L/20$, where L is the map size.

Drawing the real skeleton is rather difficult, at least we did not find yet a highly reliable algorithm. As explained in Sect. 2.1 the real skeleton is drawn by going along the trajectory with the following motion equation

$$\frac{d\mathbf{r}}{dt} \equiv \mathbf{v} = \nabla\rho, \quad (\text{A1})$$

starting from the saddle points and with initial velocity parallel to the major axis of the local curvature (the dual skeleton is obtained similarly by making the operation $\rho \rightarrow -\rho$). This equation of motion is solved numerically with a semi-implicit scheme which guaranties that the gradient does not change sign along the direction of motion. This allows as a consequence a correct calculation of the skeleton length since backwards motion along the trajectory is prevented.

More explicitly, if $\mathbf{r}_i, \mathbf{v}_i = \nabla\rho_i$ and dt_i are respectively the position, velocity and timestep at step i , the quantities at next step are computed as follows using an iterative procedure. The gradient $\nabla\rho$ is evaluated at the position $\tilde{\mathbf{r}}_{i+1} = \mathbf{r}_i + \tilde{\mathbf{v}}_{i+1}dt_{i+1}$ from which we deduce $\tilde{\mathbf{v}}_{i+1}$ and $s = \tilde{\mathbf{v}}_{i+1} \cdot \mathbf{v}_i$. As a first guess we take $d\tilde{t}_{i+1} = dt_i$ and $\tilde{\mathbf{v}}_{i+1} = \mathbf{v}_i$. As long as $s \leq 0$ we divide the timestep $d\tilde{t}_{i+1}$ by two and recompute $\tilde{\mathbf{r}}_{i+1}$. Once $s > 0$, the quantities at time step $i+1$ are set to $dt_{i+1} = d\tilde{t}_{i+1}$, $\mathbf{v}_{i+1} = \tilde{\mathbf{v}}_{i+1}$ and $\mathbf{r}_{i+1} = \mathbf{r}_i + \tilde{\mathbf{v}}_{i+1}dt_{i+1}$. Note in addition that the time step is always chosen such that the displacement between two steps is at most of the order of a pixel.

To ensure a finite number of time steps, the motion is stopped once we reached the vicinity (typically a fraction of pixel size) of a critical point and appear to converge towards it. In principle this stopping point should always be a maximum. However, in practice we found that very rarely we could converge to a saddle point. To avoid here again an infinite number of iterations, we stop the calculation of the trajectory. Indeed, this situation happens when a field line (say A) is very close to one of the two unstable field lines converging to the saddle point (see Fig. 3). After getting close to the saddle point, the field line A should turn by approximately 90 degrees to follow closely one of the two stable field lines (say B) of the saddle point. The field line B will be drawn anyway starting from this saddle point. So visually, we should not miss anything by not drawing the end of the field line A . However, this might be a problem for estimating the skeleton length since we are missing parts of it.

Eventually, the critical points are determined as intersections of the contour lines $\partial\rho/\partial r_1 = 0$ and $\partial\rho/\partial r_2 = 0$ with the same method as used for the local skeleton. This detection method can also fail (e.g. upper left panel of Fig. 2 and 10), and some critical points can be missing, which has dramatic consequences for the building of the real skeleton.

To avoid critical situations as described above, where our algorithm for drawing the real skeleton fails, we need to smooth the fields significantly, typically with a radius at least of order of 10 pixels but this depends strongly on the nature of the field.